

Entropy-Increase Assisted Anti-Sintering for Synthesis of High-Loaded Pt Intermetallic Compounds as Electrocatalysts in PEMFCs

Yongyu Pan, Yihe Chen, Yuze Li, Mengyuan Liu, Longpin Yao, Hao Zhao, Xiaoyu Zhao, Zhouying Yue, Shunjie Gui, Yubin Chen,* Qingqing Cheng,* and Hui Yang*

High-loaded Pt intermetallic compounds (IMCs) present the practical application potential in low-Pt PEM fuel cells while ordering transformation under high temperature inevitably leads to severe sintering of high-density IMC nanoparticles (NPs), thus the decayed oxygen reduction reaction (ORR) performance. Herein, an entropy-increase assisted anti-sintering concept is proposed to fundamentally reduce the surface energy of NPs by increasing the mixing entropy, thus hindering the migration and coalescence of NPs. Ex/in situ electron microscopy and density functional theory (DFT) corroborate that the higher the entropy of pristine NPs, the lower the surface energy, the smaller the average size, and the more uniform distribution after annealing. The prepared Pt high-entropy IMC (Pt-HEI@Pt/C) demonstrates high metal loading (40.53 wt.%) and small particle size (≈ 3.15 nm), which endow it with an excellent ORR activity with mass activity (MA@0.9V, $0.65 \text{ A mg}^{-1}_{\text{Pt}}$) and durability over 20k potential-cycling. Membrane electrode assembly integrated with this catalyst delivers a peak power density of 0.96 W cm^{-2} and an exceptional stability (12.5% decline in MA) under H₂-air condition at $0.1 \text{ mg}_{\text{Pt}} \text{ cm}^{-2}$. DFT reveals the reinforced strain regulation effect of the HEI core on the Pt shell, which optimizes the *OOH adsorption and elevates the energy barrier of Pt dissolution, thus simultaneously enhancing the intrinsic ORR activity and durability.

1. Introduction

Proton exchange membrane fuel cells (PEMFCs), widely recognized for their remarkable efficiency and environmental sustainability, represent a revolutionary solution in advancing global clean energy technologies.^[1,2] Nevertheless, the oxygen reduction reaction (ORR) with sluggish kinetics necessitates a high usage of Pt catalysts to ensure reliable performance and stability, which limits the large-scale application of PEMFCs.^[3,4] Pt-group metal free catalysts, such as transition metal doped carbon-based materials, have achieved remarkable progress in recent years.^[5-7] However, neither their ORR activity nor durability can match Pt-based catalysts, making it difficult for them to be practically applied in PEMFCs. Pt-based alloy catalysts, especially for the PtM (M = Fe,^[8] Co,^[9] Ni,^[10] etc.) intermetallic compounds (IMCs), as a representative of low-Pt catalysts, have attracted significant attention to dramatically reduce the Pt usage.^[11] Strengthened lattice contraction and strong orbital coupling effects confer the PtM IMC synergistically improved

ORR intrinsic activity and structural stability in comparison with PtM disordered alloy counterpart.^[12-15] However, the high energy barrier associated with ordering transformation necessitates high temperature treatment ($\geq 700 \text{ }^{\circ}\text{C}$) to drive the atom-diffusion and rearrangement,^[16,17] inevitably leading to severe nanoparticles (NPs) sintering. To address the above sintering issue, two mainstream anti-sintering strategies, including supporting engineering and space isolation, have been widely employed to successfully synthesize the small-sized PtM-IMC/C catalysts. The former mitigates the NPs sintering by establishing the strong metal-support interaction via doping or defect engineering. A typical work by Liang's group^[18] proposed a sulfur anchoring strategy to effectively restrict the IMC sintering even under $1000 \text{ }^{\circ}\text{C}$ through strong Pt-S interaction, obtaining the Pt-based IMCs with an average size smaller than 5 nm. Mo et al.^[19] utilized the strong interaction between PtCo and Co-N-C to anchor PtCo NPs onto the nanorod support, and control the particle size. The latter commonly employs surface coating, pore

Y. Pan, Y. Chen, Y. Li, M. Liu, L. Yao, H. Zhao, X. Zhao, Z. Yue, Y. Chen, Q. Cheng, H. Yang

Shanghai Advanced Research Institute
Chinese Academy of Science
Shanghai 201210, P. R. China

E-mail: chenyubin@sari.ac.cn; chengqq@sari.ac.cn; yangh@sari.ac.cn

Y. Pan, Y. Li, M. Liu, L. Yao, H. Zhao, X. Zhao, H. Yang
University of Chinese Academy of Science

Beijing 100049, China
Y. Chen, H. Yang

School of Physical Science and Technology
ShanghaiTech University
Shanghai 201210, P. R. China

S. Gui, H. Yang
CAHM Technology (Foshan) Co., Ltd
Foshan 528216, P. R. China

 The ORCID identification number(s) for the author(s) of this article can be found under <https://doi.org/10.1002/adfm.202503628>

DOI: 10.1002/adfm.202503628

confinement, molecule-assistant, molten salts, and sacrificial templating methods to physically inhibit NPs coalescence. For example, Chung et al.^[20] reported the *in situ* formation of an ultrathin (<1 nm) nitrogen-doped carbon shell during annealing, which effectively suppressed NPs sintering and obtained the small-sized IMCs. Vito Di Noto et al.^[21] encapsulated alloy nanoparticles with a CN shell, which played a key role in stabilizing the morphology.

The feasibility of the aforementioned anti-sintering strategies has been proved in a large number of reports, whereas most studies focus on the synthesis of PtM-IMC/C with low metal loading (≤ 20 wt.%)^[22] and high-surface-area carbon supports.^[23] For example, Xie et al.^[24] prepared an *fct*-Pt-Co@Pt/C catalyst with only ≈ 10 wt.% metal loading, producing NPs with an average size of ≈ 8 nm after thermal treatment at 600 °C. Feng et al.^[25] synthesized the low-loaded (<5 wt.%) Pt₃Fe-IMC, realizing the reduction in NPs size to ≈ 2 nm. In addition, some research groups have utilized the zeolite-based imidazolate frameworks (ZIFs) derived from highly porous carbon support to restrict the NP sintering through the confinement effect.^[26,27] Nevertheless, few research attempts to tackle the sintering difficulty in the synthesis of PtM-IMC/C catalysts with high metal loading (≥ 40 wt.%), which have been recognized as the practical catalysts in PEMFCs owing to the thin catalytic layer, high electron conductivity as well as the fast mass-transport.^[28] Under high metal loading conditions, the inter-particle distance (d) will be dramatically shortened. According to Yin's report,^[29] when d is lower than the critical distance (d_c), the NPs are highly susceptible to severe-sintering through NPs migration-coalescence mechanisms (PMC). As a result, conventional support anchoring or space isolation strategy is difficult to efficiently prevent the NPs from sintering during the synthesis of high-loaded IMC/C catalysts. According to the Gibbs-Thomson effect,^[30] the origin of NPs sintering is that the small NPs show high curvature, which leads to high surface energy and intensified thermal motion, thus inducing the migration, coalescence, and growth of NPs through PMC or Ostwald ripening (OR) mechanism.^[31] Given the above consideration, neither the support engineering nor the space isolation strategy can fundamentally solve the sintering problem. On the basis of NPs properties, significantly reducing the surface energy of small NPs can weaken the sintering driving force, which might be a feasible idea to theoretically prevent the sintering of high-loaded PtM-IMC/C under high-temperature treatment. Noteworthily, the surface energy of small NPs depends not only on surface curvature but also on the chemical component of NPs. For instance, Yang et al.^[32] found that high-entropy alloys can significantly regulate the surface energy of alloy by modifying the chemical environment of surface atoms. Therefore, it is possible to decrease the driving force of sintering by tuning the mixing entropy (ΔS_{mix}) of small NPs and offering a novel anti-sintering strategy to synthesize high-loaded and small-sized IMC/C catalysts. Nonetheless, no relevant studies have been reported yet.

As proof of the above concept, we have synthesized a series of Pt-based alloy precursors, from PtCo binary alloy to quinary PtCoNiGaZn high-entropy alloy (HEA), with metal loadings as high as 40.53 wt.% an average diameter of ca. 1.4 nm. Calculations find that the surface energy of alloys gradually decreases with the increase in ΔS_{mix} . Interestingly, the average size of the IMCs formed after high-temperature treatment gradually de-

creased accompanied by a narrow size distribution with an increase in ΔS_{mix} of alloy precursor, definitely demonstrating the feasibility of the entropy-increase assisted anti-sintering strategy for high-loaded high-entropy intermetallic compound (HEI). *In situ* aberration-corrected electron microscopy further revealed that HEA NPs exhibited no significant migration and coalescence at high temperatures compared to the Pt NPs with similar size, providing solid evidence for the effectiveness of entropy increase on anti-sintering. As a consequence, small-sized (≈ 3.15 nm), high-loaded (40.53 wt.%), and high ordering degree (71%) PtCoNiGaZn/XC-72 HEI with Pt-rich shell (HEI@Pt/C) is successfully prepared. The membrane electrode assembly (MEA) integrated with such a HEI@Pt/C as cathode at a low Pt loading of $0.1 \text{ mg}_{\text{pt}} \text{ cm}^{-2}$ delivers a high peak power density of 0.96 W cm^{-2} and an excellent stability ($\approx 12.5\%$ decay in mass activity after 30 000 cycles accelerated stress testing). Density functional theory (DFT) calculations unraveled that the HEI core exerts a significant compressive strain regulation on the Pt shell, realizing the enhancement in both intrinsic ORR activity and structural stability. This work demonstrates that the high entropy effect can not only greatly enhance the intrinsic activity of the catalyst, but also tackle the root of NPs sintering problem at high temperatures, which provides a novel synthesis methodology for the preparation of high load IMC/C catalysts.

2. Results and Discussion

2.1. Entropy-Increase Anti-Sintering Mechanism

We employed the liquid-phase reduction method to prepare a series of Pt-based alloy precursors from binary (PtCo) to quinary (PtCoNiGaZn) with a similar NP diameter of ca. 1.4 nm (Figure S1, Supporting Information, experimental details can be seen in the supporting information). After the surface galvanic replacement and subsequent thermal-treatment, the various Pt IMCs with Pt-rich shells can be obtained (Figure 1a). The mixing entropy (ΔS_{mix}) of various precursor NPs was calculated according to the mixing entropy equation^[33] (Detailed calculation process can be seen in Supporting Information). As expected, ΔS_{mix} gradually increases with the element types of alloys (Figure 1b). Particularly, the ΔS_{mix} of the quinary alloy is higher than $1.5R$, where R is the gas constant, indicative of the formation of high-entropy alloy (HEA). Figure 1c shows the X-ray diffraction (XRD) patterns of various alloys after annealing at 900 °C. The calculated average diameters of NPs^[34] are 19.0, 15.8, 12.6, 7.4, and 4.4 nm for Pt, PtCo, PtCoNi, PtCoNiGa, and PtCoNiGaZn, respectively, demonstrating that the increasing element types in the alloys can obviously prevent the NPs from sintering. Transmission electron microscopy (TEM) images (Figure 1d; Figure S2–S5, Supporting Information) show the NPs distribution on carbon support. To be specific, Pt, PtCo, and PtCoNi samples exhibit severe NPs aggregation with the mean size of ca. 7.67, 7.56, and 6.40 nm, respectively, while the aggregation of the PtCoNiGa NPs is alleviated to some extent with an NP size of ca. 4.79 nm. Noteworthily, PtCoNiGaZn HEA presents a remarkable anti-sintering property accompanied by the smallest NP size of ca. 3.44 nm. Moreover, the NPs distribution for various samples can be visually shown in the violin plot (Figure 1e) based on TEM images (Figure S6,

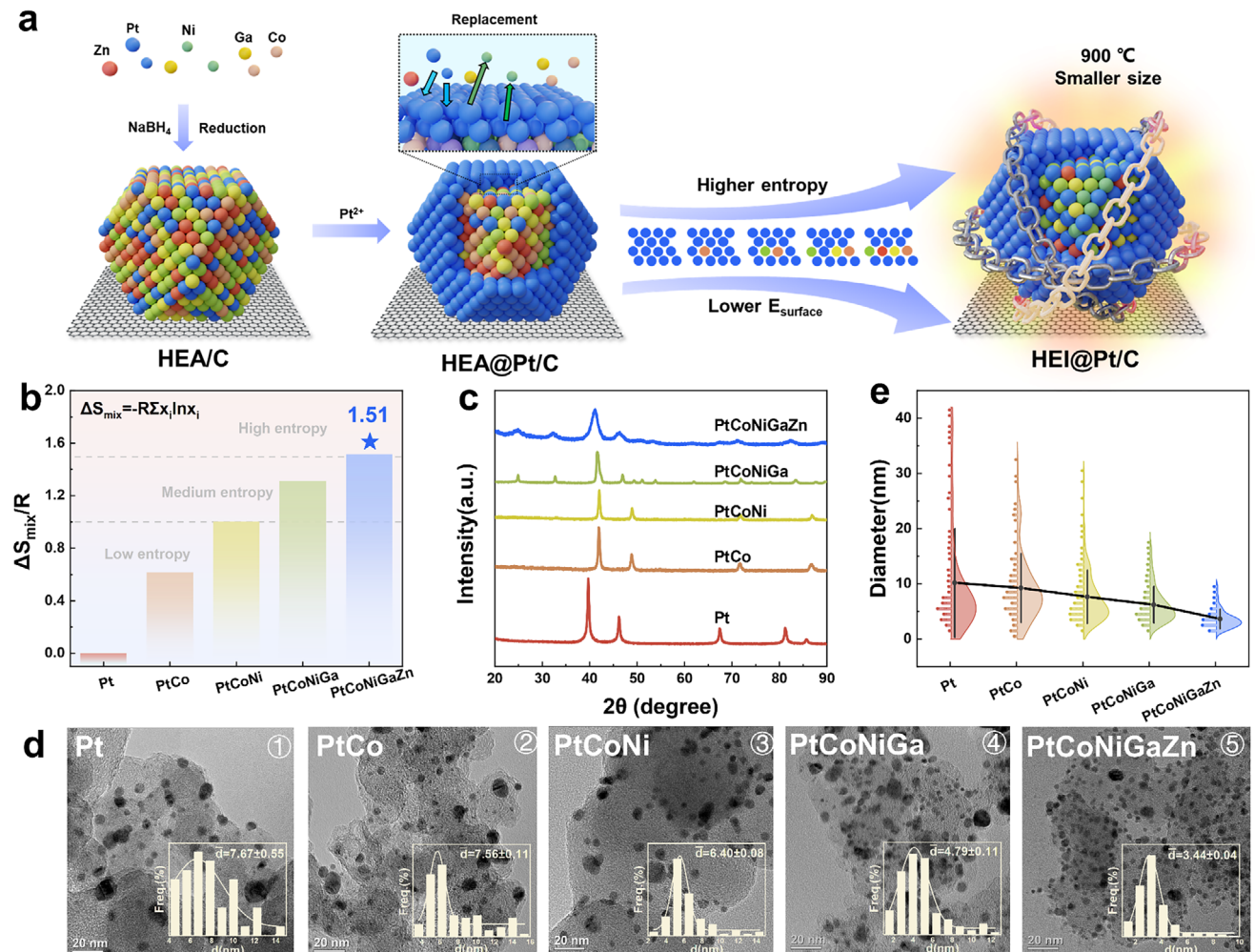


Figure 1. a) Schematic diagram of the prepared HEA/C, HEA@Pt/C and HEI@Pt/C. b) Calculated results of the mixing entropy. c) XRD patterns of Pt, PtCo, PtCoNi, PtCoNiGa and PtCoNiGaZn. d) TEM images of Pt, PtCo, PtCoNi, PtCoNiGa and PtCoNiGaZn. e) Violin plot of NPs size distribution.

Supporting Information). Clearly, the more types of metal elements, the smaller the average NP size and the more uniform the particle distribution, again proving the effectiveness of entropy increase on anti-sintering during the high-temperature ordering process.

To further clarify that the enhanced anti-sintering ability originates from the increase in configurational entropy rather than the specific chemical effects of selected elements, we introduced the metal elements with similar entropy contributions (e.g., Cu, Fe) to evaluate their influence on sintering resistance. The PtCoNi-GaCu and PtCoNiFeCu HEA control samples were prepared, which show similar ΔS_{mix} and average NPs size (Figure S7 and Table S6, Supporting Information). After annealing under the same conditions, the PtCoNiGaCu and PtCoNiFeCu samples exhibit the average size of ca. 4.10 and 3.85 nm (Figure S8, Supporting Information), similar to that of the PtCoNiGaZn. The above results demonstrate that the HEAs synthesized by replacing Ga/Zn with Cu/Fe exhibit the same anti-sintering ability, indicating that the anti-sintering ability is not attributed to the specific chemical properties of Ga and Zn. Moreover, we also prepared the PtGaZn low-entropy alloy (LEA), which shows obvi-

ous sintering behavior (with the NP size from 3.4 to 19.7 nm, calculated from XRD patterns, Figure S9, Supporting Information) after high-temperature annealing, again attesting that the increased mixing entropy other than specific element contributes to the improved anti-sintering ability.

In situ aberration-corrected scanning transmission electron microscopy (AC-STEM) experiments were performed to monitor the agglomeration behavior of NPs under high temperatures. As shown in Figure 2a, HEA NPs display a slight migration at 850 °C for 60 min (More evidence can be found in Figures S10 and S11, Supporting Information). On the contrary, Pt NPs continue to migrate and fuse at high temperatures and finally form large NPs. (Figure 2a,b; Videos S1 and S2, Supporting Information, experimental details can be seen in the Supporting Information). Concretely, the number of Pt NPs in the circled region decreases rapidly from 12 to 5 at the initial 15 min, subsequently, the #4 NP grows from 6 to 16 nm through the coalescence with other NPs during 15 to 60 min. Clearly, we observe that particles A and B migrated and aggregated into particle C within 15 min, accompanied by particle growth (More evidence of aggregation can be found in Figure S12, Supporting Information). In

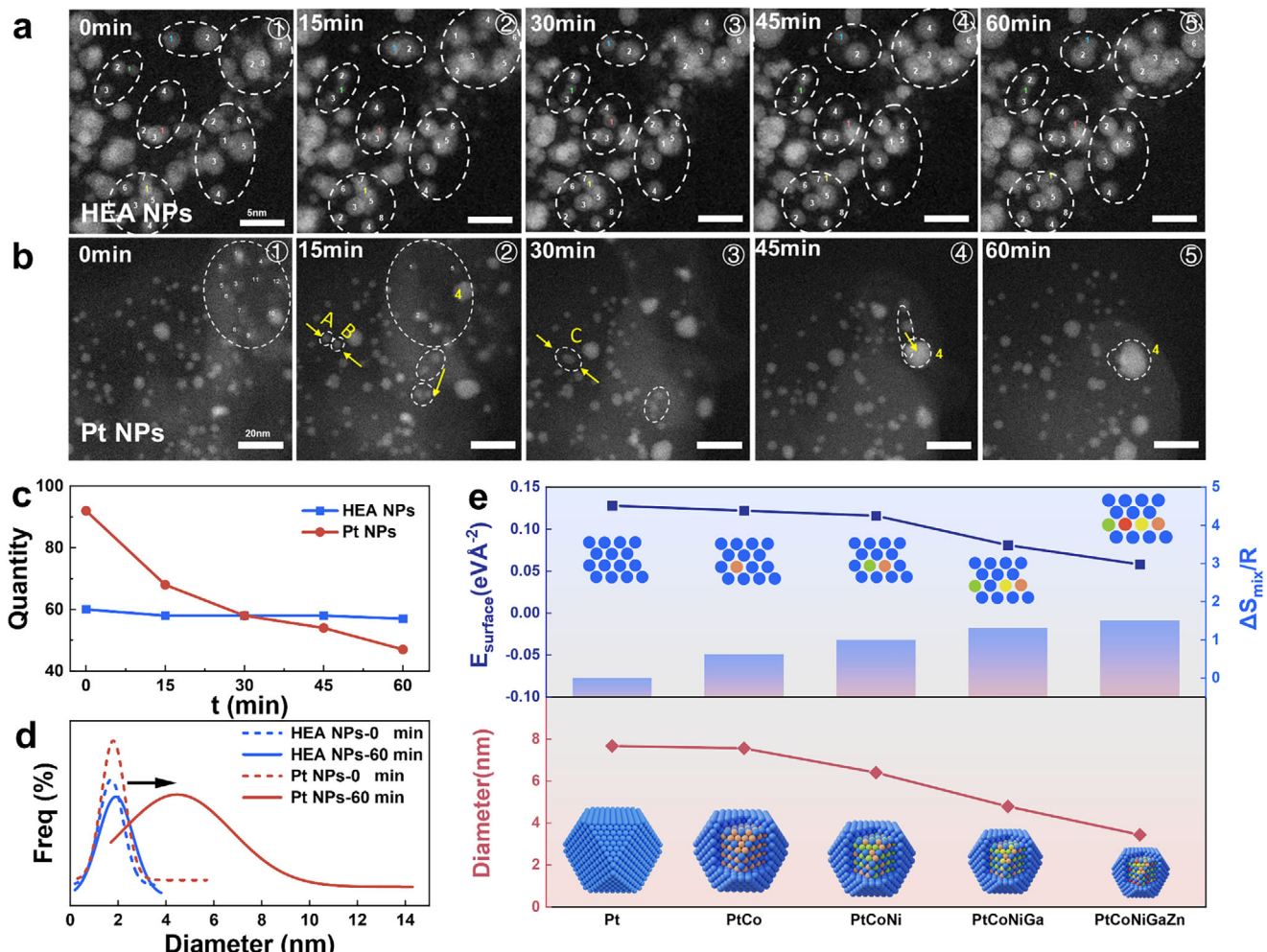


Figure 2. In situ AC-STEM images of a) HEA NPs and b) Pt NPs at 0, 15, 30, 45, and 60 min heat-treated at 850 °C. c) Particle number statistics of HEA NPs and Pt NPs from 0 to 60 min. d) Fitted curve of particle size distribution statistics of HEA NPs and Pt NPs from 0 to 60 min. e) The relationship among the surface energy (E_{surface}), mixing entropy (ΔS_{mix}), and particle size.

addition, we further analyzed the variation of NPs number and size distribution (Figures S13 and S14, Supporting Information) with annealing time. Figure 2c shows that the number of HEA NPs remains nearly constant, whereas that of Pt NPs exhibits a dramatic decrease. Meanwhile, the average size of HEA NPs remains constant at ≈ 2.0 nm with a narrow distribution, while that of Pt NPs increases from ≈ 2.3 to ≈ 5.5 nm with a broad distribution (Figure 2d). The above results solidly confirm the superiority of entropy-increase in anti-sintering during the high-temperature ordering process.

To gain insight into the entropy-increase assisted anti-sintering mechanism, we calculated the surface energy of model structures (Figure S15, Supporting Information) for various Pt alloys. As plotted in Figure 2e, the calculated surface energy decreases monotonically with an increase in ΔS_{mix} , implying that it is feasible to regulate the surface energy of small NPs by changing the components of alloys. According to Gibbs-Thomson Equation,^[35] surface energy is the driving force for the sintering of NPs under high temperatures. Therefore, the increased entropy for the alloy NPs fundamentally prevents the NPs from migra-

tion, realizing the formation of small-sized HEI NPs with high metal loading.

2.2. Physical and Electronic Structure

To confirm the formation of the IMCs, XRD patterns were compared among the synthesized HEA@Pt/C, HEI@Pt/C, and Pt/C first (Figure 3a). In contrast to commercial Pt/C, the XRD peaks of the Pt (111) plane of HEA@Pt/C and HEI@Pt/C shift to high angles (Pt/C: 39.76°, HEA@Pt/C: 40.84°, HEI@Pt/C: 41.14°), indicative of the lattice contraction induced by the transition metal (Co, Ni, Ga, and Zn) dopant. After annealing at 900 °C, the HEI@Pt/C exhibits the distinct superlattice peaks, located at 24.89° and 32.31°, corresponding to the (001) and (110) facets, respectively, confirming the formation of IMC structure. Meanwhile, the calculated ordering degree of HEI@Pt/C is as high as $\approx 71\%$, which is conducive to enhancing the ORR performance. (Detailed calculation process can be seen in the Supporting Information). As far as HEI@Pt/C is concerned, a low magnitude

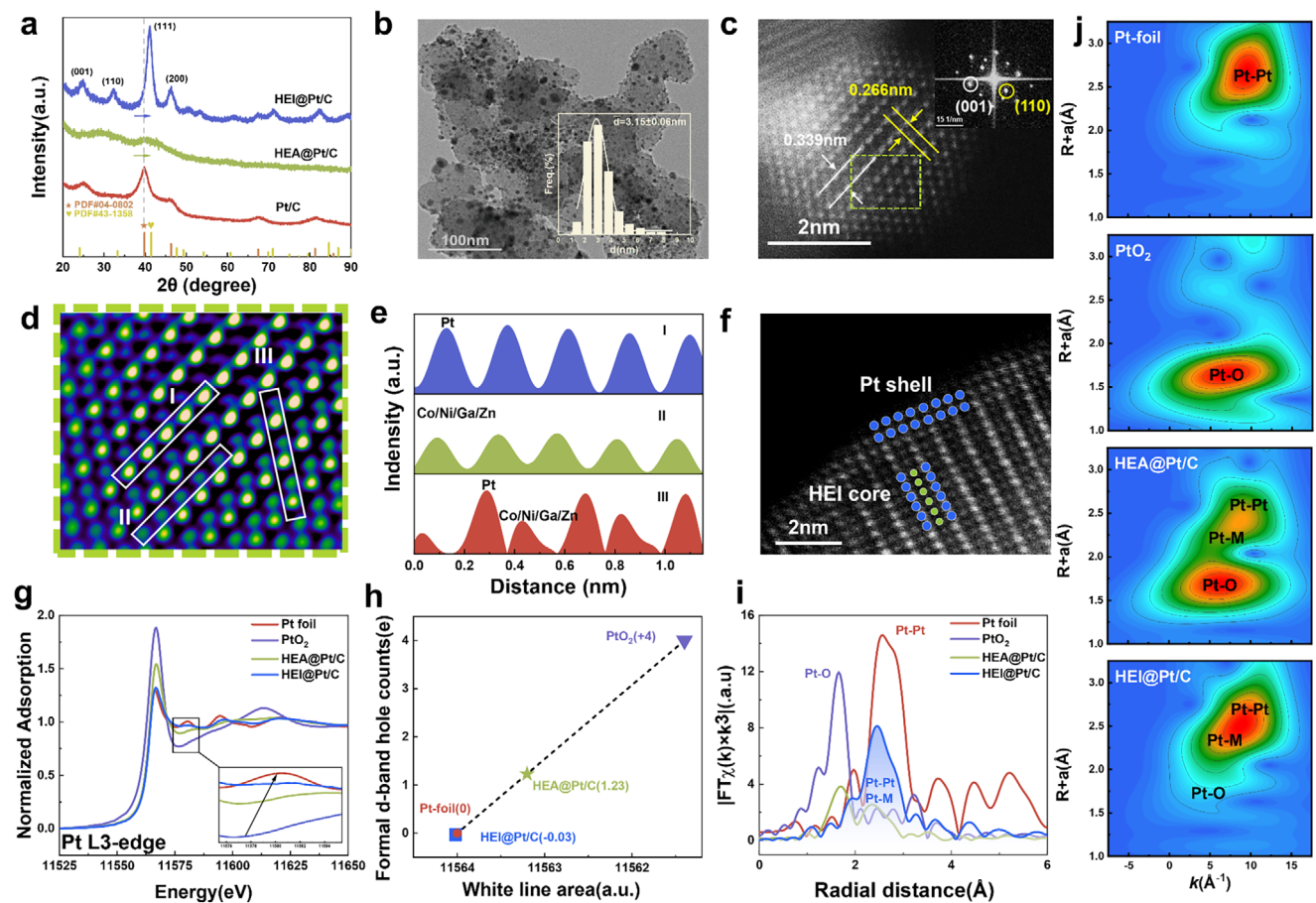


Figure 3. a) XRD patterns of the obtained HEA@Pt/C, HEI@Pt/C, and commercial Pt/C. (b) Low-magnitude TEM image of HEI@Pt/C (Inset is the corresponding particle size distribution histogram). c) Atomic-resolution HAADF-STEM image of the HEI@Pt/C and FFT image (inset) d) Enlarged HAADF-STEM image of the green square in(c) after inverse FFT. e) Line-scanning profiles in (d) of areas I, II, III. f) Atomic-resolution HAADF-STEM image of HEI@Pt/C showing an HEI core/Pt shell structure; Pt and Co atoms are blue and green, respectively g) Pt L3-edge normalized XANES spectra of Pt foil, PtO₂, HEA@Pt/C and HEI@Pt/C. h) Calculated Pt oxidation states derived from ΔXANES spectra of Pt foil, PtO₂, HEA@Pt/C, and HEI@Pt/C. i) Corresponding FT-EXAFS curves of (g). j) Pt L3-edge WT-EXAFS contour plots of Pt foil, PtO₂, HEA@Pt/C and HEI@Pt/C.

TEM image (Figure 3b) shows that the NPs are highly dispersed on carbon support with an average diameter of ca. 3.15 nm. Considering the metal loading is determined to be 40.53% by Inductively Coupled Plasma-Optical Emission Spectrometer (ICP-OES, Table S2, Supporting Information), such an HEI@Pt/C catalyst is one of the smallest IMC NPs reported to date.^[36–38] Moreover, aberration-corrected high-angle annular dark field scanning transmission electron microscopy (AC-HAADF-STEM) was conducted to observe the detailed atomic arrangements in the HEI@Pt/C nanocrystals. Figure 3c shows a typical Z-contrast atomic-resolution STEM image of a single HEI@Pt/C NPs. Obviously, Pt (bright atoms) and transition metal atoms (dark atoms) alternately stack in one direction, and line-scanning profiles in the enlarged FFT fake image (Figure 3d,e) show the alternatively varying intensities across regions I, II, and III, which prove the formation of L_{10} -face centered tetragonal (*fct*) IMC structure. The d-spacings of ca.0.339 and 0.226 nm for the adjacent lattice fringe, calculated from the AC-STEM image, matches well with that of the (001) and (110) facets of *fct* IMC structure. In addition, the superlattice reflections are also clearly observed in the fast Fourier transform (FFT) pattern (inset in Figure 3c), further evi-

dencing the formation of ordered HEI. Of note that, HEI@Pt/C NP exhibits an apparent Pt-shell with two atomic layers, covering the HEI core, demonstrating the formation of core-shell structure during the galvanic replacement step. Such HEI core @ Pt-shell structure can also be discernible in the STEM-EDS line profiles of single NPs (Figure S16, Supporting Information). EDS-mapping images (Figure S17, Supporting Information) of a single HEI NP display the uniform distribution of Pt, Co, Ni, Zn, and Ga elements, verifying the formation of homogeneous HEI. Particularly, the Pt map area is slightly larger than that of other transition metals maps, also indicating that a Pt-rich shell is formed at the surface of the ordered HEI core.

X-ray adsorption spectroscopies (XAS) were further conducted to elucidate the electronic state and the local coordination environment for the as-prepared catalyst. The normalized X-ray absorption near edge structure (XANES) (Figure 3g) indicates that the white line (WL) energy feature at the Pt L3-edge of HEI@Pt/C is obviously lower than that of HEA@Pt/C and PtO₂, but very similar to that of Pt foil, indicating that the valence state of Pt in HEI@Pt/C approaches to metallic Pt, which is reported to be more favorable for ORR catalysis.^[39] It is noting that the

inset in Figure 3h reveals an increasing intensity of the oscillation hump from HEA@Pt/C to HEI@Pt/C in the energy range from 11,576 to 11,584 eV, manifesting the phase transformation from disordered HEA to the structurally ordered HEI.^[40,41] To quantitate the valence state, the white-line peak of Pt L3-edge can be clearly described by the differential XANES spectra (Δ XANES, Figure S18, Supporting Information) by subtracting the spectra from that of Pt foil. The valence state of Pt can be quantitatively examined by the integration of white-line area in XANES spectra.^[42,43] As shown in Figure 3h, the average valence state of Pt in HEI@Pt/C is \approx 0.03, which is attributed to the electron transfer from low electronegativity atoms (Co/Ni/Ga/Zn) to Pt.^[33,44,45] Fourier transforms (FTs) of extended X-ray absorption fine structure (EXAFS) spectra (Figure 3i) exhibit a dominant peak near 2.27 Å corresponding to the Pt-M interatomic distance (Figure S19, Supporting Information). In comparison with Pt foil, the Pt-M coordination distance is significantly shortened due to the doping of smaller Co/Ni/Ga/Zn atoms into the Pt lattice. Notably, HEA@Pt/C exhibits a distinct peak at \approx 1.68 Å, which corresponds to the Pt-O coordination, implying that the Pt atoms in HEA@Pt/C could be oxidized more easily (Figure S19 and Table S4, Supporting Information). On the contrary, almost no discernable Pt-O interactions can be detected in HEI@Pt/C, demonstrating the excellent property of anti-oxidation. Additionally, wavelet transform (WT) of the Pt L3-edge EXAFS oscillations (Figure 3j) reveals that the intensity maximal of HEI@Pt/C displays a clearly negative shift comparison with Pt foil from 9.55 to 8.85 Å⁻¹, which is associated with the Pt-M contributions. Beyond that, as a comparison with PtO₂ reference, no Pt-O intensity maximal is observed, again attesting to the oxygen-resistance property for HEI@Pt/C structure.

2.3. ORR Electrocatalysis and MEA Application

Cyclic voltammogram (CV) and linear sweep voltammogram (LSV) under a three-electrode system using a rotating disk electrode (RDE) were conducted to evaluate the ORR performance of the synthesized Pt/C, PtCo/C, HEA@Pt/C, and HEI@Pt/C catalysts in 0.1 M HClO₄ solution. Based on the hydrogen underpotential deposition (UPDH) area (Figure S20, Supporting Information), the electrochemical surface area (ECSA) of the HEI@Pt/C sample is ca. 64.4 m² g⁻¹ Pt, which approaches the Pt/C with a value of 70.6 m² g⁻¹ Pt, corroborating the successful synthesis of the small-sized HEI@Pt/C NPs. ECSAs based on the CO-stripping voltammetry (Figure S21, Supporting Information) further support the above claim. However, binary PtCo-IMC/C exhibits an extremely low ECSA (32.5 m² g⁻¹ Pt), definitely assessing the positive effectiveness of entropy-increase on anti-sintering. LSVs on different catalysts (Figure 4a) indicate that the HEI@Pt/C exhibits the most positive half-wave potential ($E_{1/2}$) compared to Pt/C, PtCo/C and HEA@Pt/C. Specifically, as shown in Figure 4b, the mass activity (MA @ 0.9 V vs. RHE, normalized to the mass of Pt) and the specific surface area activity (SA @ 0.9 V vs. RHE, normalized to ECSA) for the HEI@Pt/C are 0.65 A mg⁻¹ and 1.01 mA cm⁻², which are 5.4 and 5.9 times higher than those of the commercial Pt/C with the values of 0.12 A mg⁻¹ and 0.17 mA cm⁻², respectively. Tafel analysis was used to study the ORR kinetics on various catalysts. As shown

in Figure 4c, the HEI@Pt/C displays the smallest Tafel slope of 62.2 mV dec⁻¹, further validating the greatly accelerated ORR kinetics by the construction of ordered HEI@Pt structure. Collectively, the above electrochemical results confirm the superiority of ordered HEI@Pt structure in promoting ORR electrocatalysis.

Accelerated durability tests (ADT) were performed to estimate the durability of the prepared HEI@Pt/C catalyst. As shown in Figure 4d and Figures S22 and S23 (Supporting Information), the HEI@Pt/C displays a \approx 14 mV decay in $E_{1/2}$, which is much lower than that of Pt/C (\approx 70 mV). Impressively, the MA and SA (Figure 4e) decrease by 27.0% and 12.2%, respectively. Such excellent durability primarily originates from the HEI structure that combines the slow-diffusion effect of HEA with the stabilization effect of ordered IMC. Moreover, after the stability test, NPs size and IMC structure of HEI@Pt/C are well preserved (Figures S24 and S25, Supporting Information). In contrast, commercial Pt/C exhibits severe NPs agglomeration after ADT due to the Ostwald ripening process (Figure S26, Supporting Information). In addition, we measured the Pt content in the electrolyte after ADT using ICP-MS and converted it into the Pt mass fraction (Figure S27, Supporting Information). For the HEI@Pt/C, the Pt content decreases from 26.85% to 25.63%, indicative of the stabilization effect of the HEI core on the Pt shell. In contrast, for the Pt/C, the Pt content drops from 39.89% to 24.08%, demonstrating a severe dissolution of Pt atoms. Therefore, the prepared HEI@Pt/C catalyst exhibits substantially enhanced ORR intrinsic activity as well as electrochemical durability (Figure 4f), demonstrating the superiority of HEI in catalyzing the ORR as comparison with commercial Pt/C or binary Pt-IMC catalysts.

To assess the application potential of the HEI@Pt/C in PEMFCs, the membrane electrode assembly (MEA) was prepared with a low Pt loading of 0.1 mg Pt cm⁻² as the cathode to evaluate its performance by comparing it with the commercial 40 wt.% Pt/C catalyst. The steady-state polarization curves (Figure 4g) under H₂-air conditions show that the MEA-HEI@Pt/C exhibits higher voltage at various current densities than MEA-Pt/C, indicative of an enhancement in ORR activity. Particularly, the peak power density of the MEA-HEI@Pt/C reaches as high as 0.96 W cm⁻², which exceeds that of MEA-Pt/C (0.84 W cm⁻², cathode: 0.1 mg Pt cm⁻²). Notably, at a cell voltage of 0.80 V, the current density on the MEA-HEI@Pt/C reaches 0.27 A cm⁻², which is very close to the Department of Energy (DOE) target (0.3 A cm⁻²), while significantly higher than that of Pt/C one (0.1 A cm⁻²). More importantly, at a rated working voltage, e.g., 0.65 V, the MEA-HEI@Pt/C delivers the current density of 1.11 A cm⁻², much higher than that of Pt/C (0.56 A cm⁻²), elucidating that the reduction of Pt usage never compromises the output power and suggesting the practical application potential in PEMFCs. At a cell voltage of 0.9 V, the MA of HEI@Pt/C is 0.51 A mg⁻¹, significantly higher than that of Pt/C (0.18 A mg⁻¹), demonstrating that the HEI@Pt/C catalyst also exhibits the greatly enhanced ORR activity even under fuel cell working conditions. For a better investigation of the ORR kinetics under MEA configuration, we collected the polarization curves at low current densities (\leq 100 mA cm⁻²) and calculated the Tafel slopes for both MEA-HEI@Pt/C and MEA-Pt/C. As shown in Figure S28 (Supporting Information), the MEA-HEI@Pt/C exhibits a smaller Tafel slope than Pt/C, confirming the significantly enhanced ORR kinetics enabled by the construction of the ordered HEI@Pt structure.

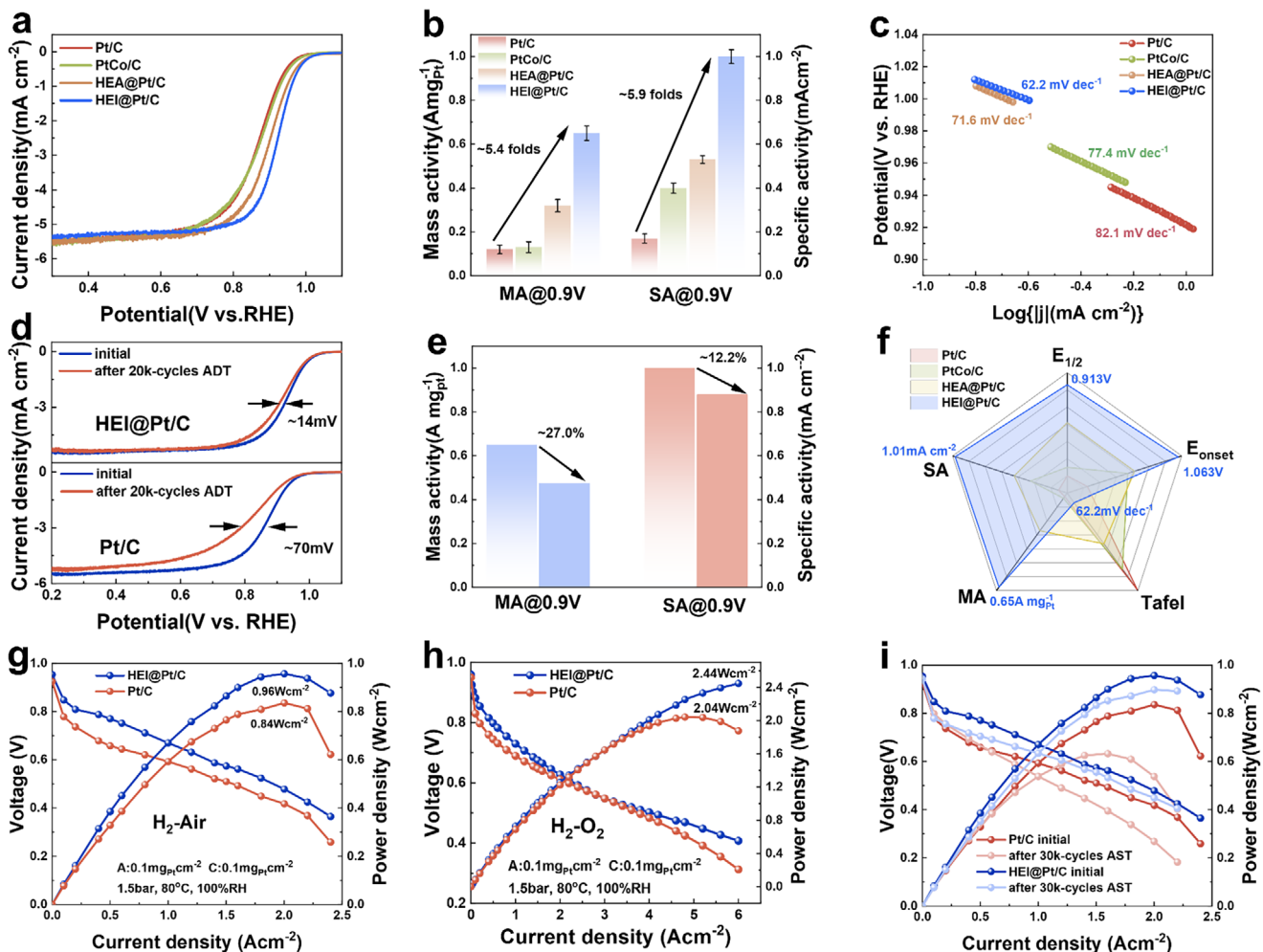


Figure 4. a) LSVs of the ORR on Pt/C, PtCo/C, HEA@Pt/C, and HEI@Pt/C, b) MA and SA of Pt/C, PtCo/C, HEA@Pt/C, and HEI@Pt/C, c) Tafel plots of Pt/C, PtCo/C, HEA@Pt/C, and HEI@Pt/C, d) Comparison of LSVs of Pt/C and HEI@Pt/C, before and after ADT e) Comparison of MA and SA of HEI@Pt/C before and after ADT f) Comparison of performance metrics of various catalysts prepared in this study, Steady-state polarization curves of MEAs with HEI@Pt/C and Pt/C as the cathode under H₂-air (g) and H₂-O₂ (h) conditions, i) Comparison of steady-state polarization curves of the HEI@Pt/C and Pt/C before and after AST.

In addition, the HEI@Pt/C reaches a power density of 2.44 W cm⁻² under H₂-O₂ fuel cell condition (Figure 4h), which surpasses the MEA-Pt/C (2.04 W cm⁻²), again evidencing the boosted ORR kinetics. Simultaneously, the MA @ 0.9 V vs. RHE of HEI@Pt/C reaches as high as \approx 0.58 A mg_{Pt}⁻¹, which is higher than that of the DOE target (0.44 A mg_{Pt}⁻¹), signifying the excellent activity expression for the high-loaded HEI@Pt/C catalyst under operating conditions. According to the DOE accelerate stability test (AST) protocol, the potential cycling on the MEA between 0.60 and 0.95 V was conducted to assess the stability of H₂-air PEMFC. After 30k-cycles AST (Figure 4i), the MEA-HEI@Pt/C exhibits a low voltage drop at different current densities compared to commercial Pt/C. Noteworthy, the peak power density of the MEA-HEI@Pt/C decreases by only \approx 6% from 0.96 to 0.90 W cm⁻², while the peak power density of MEA-Pt/C decreases by \approx 28% from 0.84 to 0.63 W cm⁻². The MA of HEI@Pt/C decreases by only \approx 12.5% and the ICP results show that the Pt loss (Figure S27, Supporting Information) within the

MEA cathode of MEA-HEI@Pt/C is only 6.7%, compared to 44.1% for the MEA-Pt/C, indicating that the HEI@Pt/C exhibits excellent long-term stability in practical applications of PEMFCs.

2.4. DFT Calculations

DFT calculations were employed to reveal the enhancement mechanism of ORR performance for the ordered HEI@Pt/C catalyst. According to the experimental results, we constructed the core-shell model for HEI@Pt featuring two atomic layers of Pt shell and HEI core. For comparison, we also established the binary PtCo@Pt model (Figure S29, Supporting Information). As illustrated in Figure S29 (Supporting Information), the Pt-Pt distances ($d_{\text{Pt-Pt}}$) in the shells of PtCo@Pt and HEI@Pt are 2.69 and 2.57 Å, demonstrating the varying degrees of compressive strain for PtCo@Pt (3.05%) HEI@Pt (7.38%), respectively. The electron localization function (ELF, Figure 5a; Figure S30,

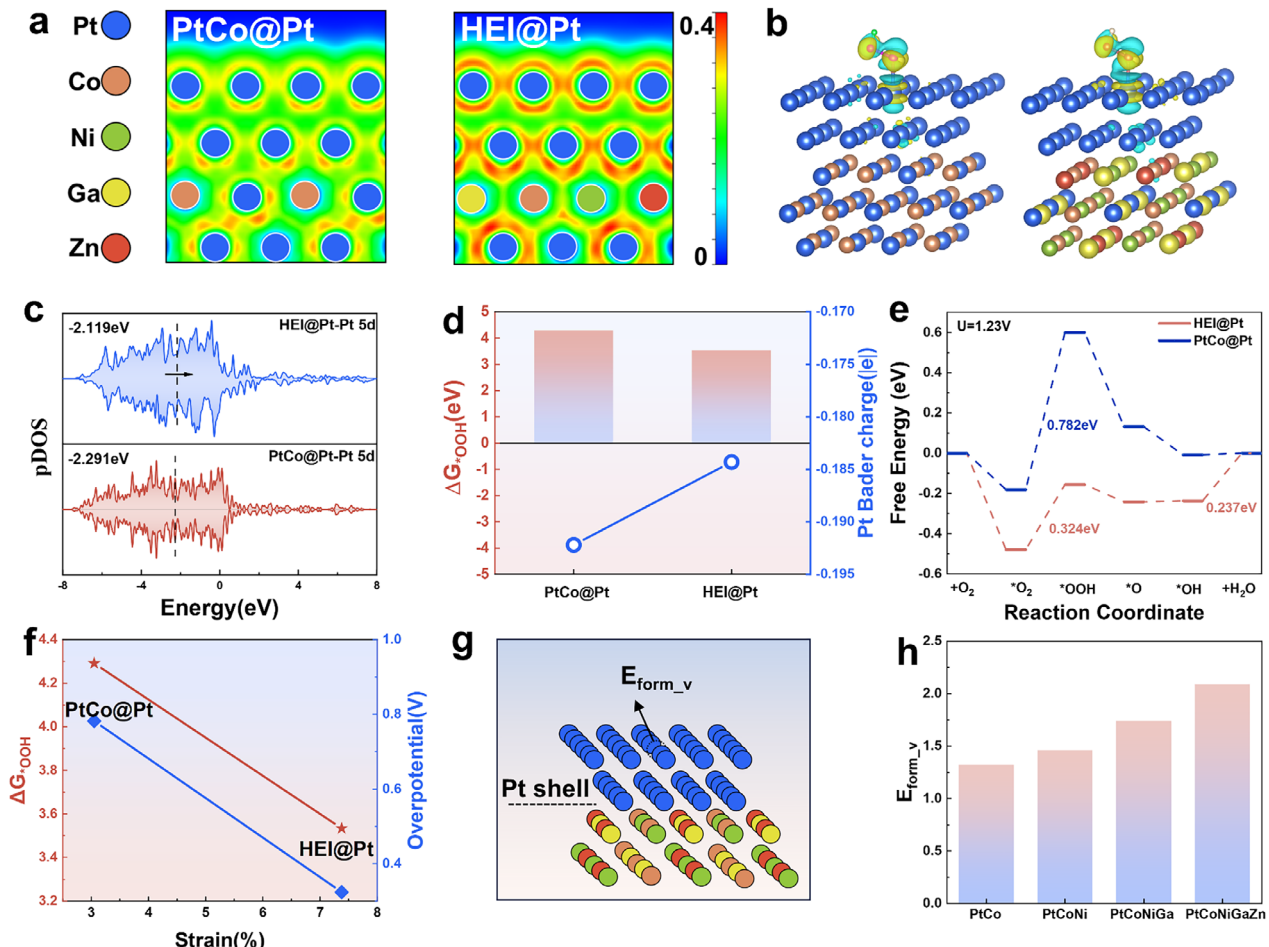


Figure 5. a) 2D display of the electron localization function (ELF) analysis for the PtCo@Pt and HEI@Pt. b) Calculated electron density distribution of active centers in PtCo@Pt and HEI@Pt and iso-surfaces represent the electron accumulation and depletion, respectively. c) pDOS of Pt-5d on Pt, PtCo@Pt and HEI@Pt models. d) The relationship between ΔG_{*OOH} and Bader charge of PtCo@Pt and HEI@Pt. e) The free energy diagrams of ORR at $U = 1.23$ V on HEI@Pt and PtCo@Pt models. f) Correlation analysis among strain, ΔG_{*OOH} and overpotentials of ORR on PtCo@Pt and HEI@Pt. g) Schematic diagram of vacancy-mediated diffusion of Pt. h) Vacancy formation energy (E_{form_v}) of surface Pt atoms.

Supporting Information) shows more electron transfer from the HEI core to the outer Pt shell HEI@Pt in contrast to PtCo@Pt. The charge density difference distribution and Bader charge calculations (Figure 5b,d) also present that the Bader charge on Pt shell in HEI@Pt ($-0.184|\text{e}^-|$) is obviously higher than that in PtCo@Pt ($-0.192|\text{e}^-|$).^[46,47] The above electronic structure analysis revealed that the intensified compressive strain induces the strong d-orbital coupling and strength of the electronic interaction between the HEI core and Pt shell.^[48] Moreover, the projected density of state (pDOS) was employed to obtain the detailed adsorption behavior on the Pt shell (Figure 5c). Of note that, the d band center of Pt shell in HEI@Pt is an upward shift by 0.172 eV as comparison with PtCo@Pt (111), indicating the strengthened interaction between adsorbate and Pt atom, which is reported to be beneficial for the absorption of OOH* via decreasing the occupation of antibonding orbitals,^[49] thus boosting the ORR kinetics. Specifically, the ΔG_{*OOH} of the HEI@Pt is close to the top of the volcano compared to that of PtCo@Pt (Figure S31, Supporting Information),^[50] thus exhibiting superior ORR performance. The Gibbs free energy diagrams for the HEI@Pt and PtCo@Pt

(Figure 5e) show that HEI@Pt exhibits a lower energy barrier (0.324 vs. 0.782 eV) of rate-determining step at 1.23 V vs. RHE than PtCo@Pt, implying the improved intrinsic activity for the HEI@Pt.^[51] The above results indicate that electron enrichment on Pt atoms optimizes the chemical adsorption of intermediates by modulating the d-band center, thereby enhancing the ORR activity.

In addition, the relationship between ΔG_{*OOH} , overpotential, and compressive strain was presented in Figure 5f. It is noted that the HEI@Pt exhibits the maximum compressive strain, inducing the lowest ΔG_{*OOH} and ORR overpotential, revealing the reasons for the excellent ORR activity.^[52] Moreover, the mechanism of the stability enhancement for HEI@Pt was explored. Given that Pt surface dissolution is mainly responsible for the catalyst deactivation,^[53] the vacancy formation energies of the surface Pt atom were calculated (Figure 5g,h; Figure S32, Supporting Information). It is observed that the vacancy formation energies of surface Pt in PtCo, PtCoNi, PtCoNiGa, and PtCoNiGaZn are 1.32, 1.46, 1.74, and 2.09 eV, respectively, demonstrating that the HEI core protects the outer Pt against

dissolution during the ORR, interpreting the excellent electrochemical durability.

3. Conclusion

In summary, we propose an “entropy-increase assisted anti-sintering” strategy to successfully synthesize the high-loaded (40.53 wt%) and small-sized (3.15 nm) Pt-HEI@Pt/C catalyst. The key finding is that by increasing compositional and configurational entropy of the alloy precursor NPs, the migration and aggregation of high-loading alloy NPs on carbon support can be effectively inhibited during the high-temperature ordering process, thus facilitating the formation of small-sized, highly ordered Pt-HEI/C. XRD, ex/in situ electron microscopy, and theoretical calculations further confirm that the increase in alloy precursor entropy significantly reduces the surface energy of NPs, thereby weakening the driving force for NPs sintering at high temperatures. The prepared PtCoNiZnGa-IMC@Pt catalyst achieves high peak-power densities of 2.44/0.96 W cm⁻² under H₂-O₂/air conditions while reducing the cathodic Pt usage as low as 0.1 mg_{Pt} cm⁻². DFT calculations uncover that the HEI core exerts a strong compressive strain effect on the surface Pt shell, which optimizes the adsorption of key oxygen intermediates and hence improves the ORR activity. This study not only offers a new concept to fundamentally inhibit the NPs sintering under high temperature but also provides an ideal approach to synthesize high-loaded and small-sized Pt-IMCs/C catalysts toward the ORR, laying the foundation for the future development of low-Pt fuel cells.

4. Experimental Section

Synthesis of PtCoNiGaZn/C (HEA/C) Nanoparticles: In a typical synthesis of HEA/C, 0.125 g K₂PtCl₆, 0.084 g CoCl₂, 0.12 g NiCl₂·6H₂O, 0.12 g Ga(NO₃)₃·xH₂O, 0.048 g ZnCl₂, and 0.1 g XC-72 were dissolved in 100 mL of ethylene glycol (EG) in a conical flask under continuous ultrasonication. The solution was then purged with argon (Ar) for 20 min to remove dissolved oxygen. Subsequently, 800 mg NaBH₄ was dispersed in 15 mL of ice-cold, Ar-purged water. This freshly prepared reducing agent solution was gradually introduced into the metal ion solution at a controlled rate of 3 mL min⁻¹ using a syringe. The resulting mixture was further ultrasonicated and purged with Ar for an additional 30 min to ensure a thorough reaction. Finally, the synthesized product was separated via centrifugation, washed with Ar-saturated ultrapure ethanol, and dried in a vacuum oven at room temperature for 12 h.

Synthesis of PtCoNiGaZn@Pt/C (HEA@Pt/C) Nanoparticles: To synthesize PtCoNiGaZn@Pt (HEA@Pt) NPs, HEA seeds were introduced into a 100 mL three-neck round-bottom flask containing 60 mL of ethylene glycol (EG) and 0.0415 g K₂PtCl₆. The solution was first purged with argon (Ar) for 30 min to remove dissolved oxygen. Subsequently, the reaction mixture was stirred at 60 °C for 24 h. After completion, the solution was allowed to cool to room temperature, and the resulting product was collected by centrifugation at 10 000 rpm for 5 min. The sample was then thoroughly washed with a 1:1 (vol/vol) mixture of Ar-saturated ethanol and deionized water (DI). Finally, the obtained HEA@Pt/C was stored in a glovebox under an Ar atmosphere for further characterization and electrochemical measurements.

Synthesis of PtCoNiGaZn@Pt/C Intermetallic Compound (HEI@Pt/C) Nanoparticles: The HEA@Pt catalyst was subjected to a heat treatment in a high-temperature tubular furnace under a 10% H₂/Ar atmosphere. The temperature was ramped at a rate of 10 °C min⁻¹ to 900 °C, where it was maintained for 1 h. Subsequently, the temperature was lowered at a rate of 1 °C min⁻¹ to 500 °C and held for 2 h. After natural cooling, the

catalyst was treated in 0.5 M H₂SO₄ at 60 °C for 4 h. The sample was then thoroughly washed with deionized water and dried. Finally, to eliminate surface defects, the catalyst underwent a secondary heat treatment at 200 °C for 1 h under a 5% H₂/Ar atmosphere, yielding the final HEI@Pt/C catalyst.

#Pt/C, PtCo/C, PtCoNi/C, and PtCoNiGa/C were all prepared using the above method, and the specific amounts of the materials used are provided in Table S1 (Supporting Information).

Material Characterization: XRD patterns were obtained using a Bruker AXS D8 ADVANCE powder diffractometer equipped with a CuK α radiation source ($\lambda = 1.5418 \text{ \AA}$). XANES and EXAFS spectra were measured at the BL14W1 beamline of the Shanghai Synchrotron Radiation Facility (SSRF) and analyzed using IFEFFIT Athena and Artemis software. Aberration-corrected high-angle annular dark-field scanning transmission electron microscopy (HAADF-STEM) and high-resolution transmission electron microscopy (HRTEM) images were acquired on a JEM-ARM 200F atomic resolution analytical microscope operating at 200 kV. In situ high-temperature observations were performed using a JEM-ARM 300F environmental spherical aberration-corrected transmission electron microscope (AC-TEM).

Electrochemical Characterization: Electrochemical tests were conducted using a three-electrode system with platinum wire as the counter electrode, Hg/Hg₂SO₄ as the reference electrode, and a glassy carbon electrode (0.196 cm²) as the working electrode. A CHI730E Potentiostat/Galvanostat controlled the current and voltage. A catalyst ink was prepared by dispersing 2 mg of catalyst in 1 mL of mixed solvent (deionized water: isopropyl alcohol: 5 wt.% Nafion = 0.96:1:0.04). Then, 5.7 μL of the ink was drop-cast onto a rotating disk electrode (RDE) and dried under an incandescent lamp. For catalyst activation, 200 cyclic voltammetry (CV) cycles were performed between 0.07–1.05 V (vs. RHE) at 100 mV s⁻¹ in 0.1 M N₂-saturated HClO₄. CV curves were then recorded in the same potential range at 50 mV s⁻¹. Linear sweep voltammetry (LSV) was conducted from 0.07 to 1.1 V (vs. RHE) at 10 mV s⁻¹ in 0.1 M O₂-saturated HClO₄ to evaluate catalytic activity. Accelerated durability tests (ADTs) were performed by applying 20 000 CV cycles between 0.6–1.0 V (vs. RHE) at 100 mV s⁻¹ in 0.1 M O₂-saturated HClO₄ to assess catalyst stability.

Membrane Electrode Assemblies (MEAs) Tests: The MEA device was integrated with an Arbin testing system to evaluate the catalytic performance under practical PEMFC operating conditions. First, 38.8 mg of catalyst was mixed with 5 wt.% Nafion (111.2 mg), deionized water (864.6 mg), and isopropyl alcohol (864.6 mg), followed by ultrasonic dispersion for 3 h to form a uniform ink. The ink was then sprayed onto a 12 μm thick Gore film (effective area: 6.25 cm²) using a spray gun. The cathode was coated with either HEI@Pt/C or 40% Pt/C catalyst at a loading of 0.1 mg cm⁻², while the anode was loaded with JM-60% Pt/C catalyst at 0.1 mg cm⁻². The prepared MEAs were activated and tested in a PEMFC setup by supplying H₂ to the anode at 1 standard liter per minute (slpm) and O₂ or air to the cathode at 0.4 slpm and 1 slpm, respectively. The testing temperature was maintained at 80 °C with 100% relative humidity (RH), and the backpressure was fixed at 1.5 bar.

Supporting Information

Supporting Information is available from the Wiley Online Library or from the author.

Acknowledgements

This work was supported by the National Natural Science Foundation of China (22472193), the Shanghai Science and Technology Innovation Action Plan (23ZR1471000, 22511102500), the Shanghai Rising-Star Program (24QA2710500, Shanghai Scientific and Technological Committee). The Key Research and Development Project of Guangdong Province (2023B0909060003), the BL14W1 beamline at Shanghai Synchrotron Radiation Facility, the Centre for High-Resolution Electron Microscopy (CH-EM), the ShanghaiTech University (EM02161943) and Shanghai Key Laboratory

of High-resolution Electron Microscopy, Shanghai Science and Technology Plan.

Conflict of Interest

The authors declare no conflict of interest.

Data Availability Statement

The data that support the findings of this study are available in the supplementary material of this article.

Keywords

anti-sintering, entropy increase, high-entropy intermetallic, oxygen reduction reaction, proton exchange membrane fuel cell

Received: February 9, 2025

Revised: April 27, 2025

Published online:

- [1] X. X. Wang, M. T. Swihart, G. Wu, *Nat. Catal.* **2019**, *2*, 578.
- [2] M. K. Debe, *Nature* **2012**, *486*, 43.
- [3] J. Zhao, H. Liu, X. Li, *Electrochem. Energy Rev.* **2023**, *6*, 13.
- [4] Y. Bing, H. Liu, L. Zhang, D. Ghosh, J. Zhang, *Chem. Soc. Rev.* **2010**, *39*, 2184.
- [5] J. Li, M. Chen, D. A. Cullen, S. Hwang, M. Wang, B. Li, K. Liu, S. Karakalos, M. Lucero, H. Zhang, C. Lei, H. Xu, G. E. Sterbinsky, Z. Feng, D. Su, K. L. More, G. Wang, Z. Wang, G. Wu, *Nat. Catal.* **2018**, *1*, 935.
- [6] M. Huang, X. Zhu, W. Shi, Q. Qin, J. Yang, S. Liu, L. Chen, R. Ding, L. Gan, X. Yin, *Sci. Adv.* **2025**, *11*, ads6658.
- [7] Y. He, H. Guo, S. Hwang, X. Yang, Z. He, J. Braaten, S. Karakalos, W. Shan, M. Wang, H. Zhou, Z. Feng, K. L. More, G. Wang, D. Su, D. A. Cullen, L. Fei, S. Litster, G. Wu, *Adv. Mater.* **2020**, *32*, 2003577.
- [8] D. Lai, Q. Cheng, Y. Zheng, H. Zhao, Y. Chen, W. Hu, Z. Zou, K. Wen, L. Zou, H. Yang, *J. Mater. Chem. A* **2022**, *10*, 16639.
- [9] Q. Cheng, S. Yang, C. Fu, L. Zou, Z. Zou, Z. Jiang, J. Zhang, H. Yang, *Energy Environ. Sci.* **2022**, *15*, 278.
- [10] L. Bu, Q. Shao, B. E. J. Guo, J. Yao, X. Huang, *J. Am. Chem. Soc.* **2017**, *139*, 9576.
- [11] S.-L. Xu, P. Yin, L.-J. Zuo, S.-Y. Yin, Y. Lin, W. Zhang, S.-Q. Chu, H.-W. Liang, X.-Z. Fu, *ACS Sustainable Chem. Eng.* **2023**, *11*, 12093.
- [12] L. Zou, J. Fan, Y. Zhou, C. Wang, J. Li, Z. Zou, H. Yang, *Nano Res.* **2015**, *8*, 2777.
- [13] J. Kim, Y. Lee, S. Sun, *J. Am. Chem. Soc.* **2010**, *132*, 4996.
- [14] J. Wang, F. Pan, W. Chen, B. Li, D. Yang, P. Ming, X. Wei, C. Zhang, *Electrochem. Energy Rev.* **2023**, *6*, 6.
- [15] N. Wang, C. Tang, L. Du, R. Zhu, L. Xing, Z. Song, B. Yuan, L. Zhao, Y. Aoki, S. Ye, *Adv. Energy Mater.* **2022**, *12*, 2201882.
- [16] Y. Wang, X. Lei, J. Zhao, X. Liu, L. Zhang, D. Su, *J. Mater. Res.* **2024**, *39*, 1325.
- [17] J. Zhang, L. Zhang, Z. Cui, *Chem. Commun.* **2021**, *57*, 11.
- [18] C.-L. Yang, L.-N. Wang, P. Yin, J. Liu, M.-X. Chen, Q.-Q. Yan, Z.-S. Wang, S.-L. Xu, S.-Q. Chu, C. Cui, H. Ju, J. Zhu, Y. Lin, J. Shui, H.-W. Liang, *Science* **2021**, *374*, 459.
- [19] R. Mo, X. Zhang, Z. Chen, S. Huang, Y. Li, L. Liang, Z. Q. Tian, P. K. Shen, *Int. J. Hydrot. Energy* **2021**, *46*, 15991.
- [20] D. Y. Chung, S. W. Jun, G. Yoon, S. G. Kwon, D. Y. Shin, P. Seo, J. M. Yoo, H. Shin, Y.-H. Chung, H. Kim, B. S. Mun, K.-S. Lee, N.-S. Lee, S. J. Yoo, D.-H. Lim, K. Kang, Y.-E. Sung, T. Hyeon, *J. Am. Chem. Soc.* **2015**, *137*, 15478.
- [21] V. Di Noto, E. Negro, B. Patil, F. Lorandi, S. Boudjelida, Y. H. Bang, K. Vezzù, G. Pagot, L. Crociani, A. Nale, *ACS Catal.* **2022**, *12*, 12291.
- [22] T. Chen, C. Qiu, X. Zhang, H. Wang, J. Song, K. Zhang, T. Yang, Y. Zuo, Y. Yang, C. Gao, W. Xiao, Z. Jiang, Y. Wang, Y. Xiang, D. Xia, *J. Am. Chem. Soc.* **2023**, *146*, 1174.
- [23] Z. Wu, Y. Lv, Y. Xia, P. A. Webley, D. Zhao, *J. Am. Chem. Soc.* **2012**, *134*, 2236.
- [24] M. Xie, Z. Lyu, R. Chen, M. Shen, Z. Cao, Y. Xia, *J. Am. Chem. Soc.* **2021**, *143*, 8509.
- [25] X. Feng, N. Yang, W. Zhang, W. Hong, L. Tan, F. Wang, D. Sun, W. Ding, J. Li, L. Li, Z. Wei, *Matter* **2022**, *5*, 2946.
- [26] S. Hanif, X. Shi, N. Iqbal, T. Noor, R. Anwar, A. M. Kannan, *Appl. Catal. B Environ.* **2019**, *258*, 117947.
- [27] Z. Chen, C. Hao, B. Yan, Q. Chen, H. Feng, X. Mao, J. Cen, Z. Q. Tian, P. Tsiakaras, P. K. Shen, *Adv. Energy Mater.* **2022**, *12*, 2201600.
- [28] Y. Xiong, L. Xiao, Y. Yang, F. J. DiSalvo, H. D. Abruna, *Chem. Mater.* **2018**, *30*, 1532.
- [29] P. Yin, S. Hu, K. Qian, Z. Wei, L.-L. Zhang, Y. Lin, W. Huang, H. Xiong, W.-X. Li, H.-W. Liang, *Nat. Commun.* **2021**, *12*, 4865.
- [30] S. Shahandeh, S. Natafgh, *Mater. Sci. Eng. A* **2007**, *443*, 178.
- [31] T. W. Hansen, A. T. DeLaRiva, S. R. Challa, A. K. Datye, *Acc. Chem. Res.* **2013**, *46*, 1720.
- [32] Z. Yang, X. Li, W. Gao, *Surf. Interfaces* **2023**, *42*, 103442.
- [33] Y. Li, S. Wang, X. Wang, M. Yin, W. Zhang, *J. Mater. Sci. Technol.* **2020**, *43*, 32.
- [34] U. Holzwarth, N. Gibson, *Nat. Nanotechnol.* **2011**, *6*, 534.
- [35] M. Lin, G. Gottstein, L. S. Shvindlerman, *Acta Mater.* **2017**, *129*, 361.
- [36] G. Feng, F. Ning, Y. Pan, T. Chen, J. Song, Y. Wang, R. Zou, D. Su, D. Xia, *J. Am. Chem. Soc.* **2023**, *145*, 11140.
- [37] Q. Zhang, T. Shen, M. Song, S. Wang, J. Zhang, X. Huang, S. Lu, D. Wang, *J. Energy Chem.* **2023**, *86*, 158.
- [38] J. Ma, F. Xing, Y. Nakaya, K. Shimizu, S. Furukawa, *Angew. Chem., Int. Ed.* **2022**, *61*, 202200889.
- [39] M. Luo, S. Guo, *Nat. Rev. Mater.* **2017**, *2*, 17059.
- [40] S. Fang, X. Zhu, X. Liu, J. Gu, W. Liu, D. Wang, W. Zhang, Y. Lin, J. Lu, S. Wei, Y. Li, T. Yao, *Nat. Commun.* **2020**, *11*, 1029.
- [41] S. Dai, J.-P. Chou, K.-W. Wang, Y.-Y. Hsu, A. Hu, X. Pan, T.-Y. Chen, *Nat. Commun.* **2019**, *10*, 440.
- [42] K. L. Zhou, Z. Wang, C. B. Han, X. Ke, C. Wang, Y. Jin, Q. Zhang, J. Liu, H. Wang, H. Yan, *Nat. Commun.* **2021**, *12*, 3783.
- [43] B. Ravel, M. Newville, *J. Synchrotron Radiat.* **2005**, *12*, 537.
- [44] C. Triolo, K. Moulaee, A. Ponti, G. Pagot, V. Di Noto, N. Pinna, G. Neri, S. Santangelo, *Adv. Funct. Mater.* **2024**, *34*, 2306375.
- [45] K. Vezzù, C. Triolo, K. Moulaee, G. Pagot, A. Ponti, N. Pinna, G. Neri, S. Santangelo, V. Di Noto, *Small* **2025**, *21*, 2408319.
- [46] Y. Jia, Z. Xue, J. Yang, Q. Liu, J. Xian, Y. Zhong, Y. Sun, X. Zhang, Q. Liu, D. Yao, G. Li, *Angew. Chem., Int. Ed.* **2022**, *61*, 202110838.
- [47] A. V. Kuzmin, B. A. Shainyan, *ACS Omega* **2021**, *6*, 374.
- [48] F. Kong, Y. Huang, X. Yu, M. Li, K. Song, Q. Guo, X. Cui, J. Shi, *J. Am. Chem. Soc.* **2024**, *146*, 30078.
- [49] H. Zhao, M. Liu, Q. Wang, Y. Li, Y. Chen, Y. Zhu, Z. Yue, J. Li, G. Wang, Z. Zou, Q. Cheng, H. Yang, *Energy Environ. Sci.* **2024**, *17*, 6594.
- [50] B.-H. Lee, H. Shin, A. S. Rasouli, H. Choubisa, P. Ou, R. Dorakhan, I. Grigioni, G. Lee, E. Shirzadi, R. K. Miao, J. Wicks, S. Park, H. S. Lee, J. Zhang, Y. Chen, Z. Chen, D. Sinton, T. Hyeon, Y.-E. Sung, E. H. Sargent, *Nat. Catal.* **2023**, *6*, 234.
- [51] B. Hammer, J. K. Nørskov, *Nature* **1995**, *376*, 238.
- [52] J. K. Nørskov, J. Rossmeisl, A. Logadottir, L. Lindqvist, J. R. Kitchin, T. Bligaard, H. Jónsson, *J. Phys. Chem. B* **2004**, *108*, 17886.
- [53] X. Liu, Y. Wang, J. Liang, S. Li, S. Zhang, D. Su, Z. Cai, Y. Huang, L. Elbaz, Q. Li, *J. Am. Chem. Soc.* **2024**, *146*, 2033.